Science of the Total Environment 649 (2019) 515–525

Contents lists available at ScienceDirect

Science of the Total Environment

journal homepage: www.elsevier.com/locate/scitotenv

Data-driven mapping of the spatial distribution and potential changes of frozen ground over the Tibetan Plateau

Taihua Wang, Dawen Yang *, Beijing Fang, Wencong Yang, Yue Qin, Yuhan Wang

State Key Laboratory of Hydroscience and Engineering, Department of Hydraulic Engineering, Tsinghua University, Beijing 100084, China

HIGHLIGHTS

- Statistics and machine learning methods are compared and applied on frozen ground estimation of the Tibetan Plateau.
- Permafrost and maximum thickness of seasonally frozen ground distribution are mapped over the Tibetan Plateau.
- Around 26% and 44% of the current permafrost is projected to disappear by the 2040s and 2090s under RCP 4.5 scenario.
- Decreases in maximum seasonal frozen depth are larger at higher elevation compared with the decreases at lower elevation.

GRAPHICAL ABSTRACT

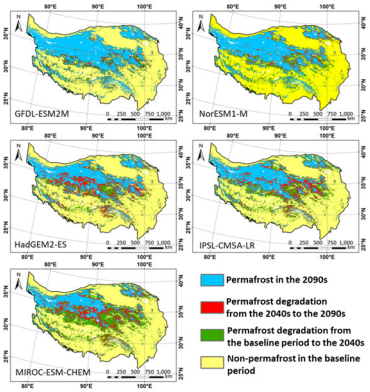

Permafrost degradation processes projected by 5 General Circulation Models under Representative Concentration Pathway 4.5

ARTICLE INFO

Article history:
Received 21 June 2018
Received in revised form 24 August 2018
Accepted 26 August 2018
Available online 28 August 2018

Editor: Jay Gan

Keywords:
Machine learning
Tibetan Plateau
Permafrost degradation
Maximum thickness of seasonally frozen ground
Climate change

ABSTRACT

Frozen ground degradation profoundly impacts the hydrology, ecology and human society on the Tibetan Plateau (TP) and the downstream regions. The spatial distribution and potential changes of permafrost and maximum thickness of seasonally frozen ground (MTSFG) on the TP is of great importance and needs more in-depth studies. This study maps the permafrost and MTSFG distribution in the baseline period (2003−2010) and in the future (2040s and 2090s) with 1-km resolution. Logistic regression (LR), support vector machine (SVM) and random forest (RF) are validated using 106 borehole observations and proved to be applicable in estimating permafrost distribution. According to the majority voting results of the three algorithms, 45.9% area of the TP is underlain by permafrost in the baseline period, and respectively 25.9% and 43.9% of the current permafrost will disappear by the 2040s and the 2090s projected by mean of the projections from the five General Circulation Models under the Representative Concentration Pathway 4.5 scenario. SVM performs better in spatial generalization than RF based on the results of nested cross validation. According to the MTSFG results derived from SVM, the most dramatic decrease in MTSFG will occur in the southwestern TP, which is projected to exceed 50 cm in the 2090s compared with the baseline period. This study introduces the statistics and machine learning algorithms to frozen ground estimation on the TP, and the high resolution permafrost and MTSFG maps produced by this study can provide useful information for future studies on the third pole region.

© 2018 Elsevier B.V. All rights reserved.

* Corresponding author.
E-mail address: yangdw@tsinghua.edu.cn (D. Yang).

https://doi.org/10.1016/j.scitotenv.2018.08.369
0048-9697/© 2018 Elsevier B.V. All rights reserved.

1. Introduction

Permafrost is defined as the sub-surface material having a temperature of less or equal to 0 °C during at least two consecutive years (Gruber, 2012). The Tibetan Plateau (TP), also known as the third pole of the globe, has the largest area of alpine permafrost in the world (Qiu, 2008; Immerzeel et al., 2010; Cuo et al., 2015). As climate warms, the active layer thickness increases and the permafrost disappearance have been reported on the TP (Li et al., 2008; Wu et al., 2015; Luo et al., 2016). In addition to permafrost, the regions with absence of permafrost include seasonally frozen ground region which freezes and thaws annually, as well as unfrozen ground which never freezes. The maximum thickness of seasonally frozen ground (MTSFG) decreased continuously in the past decades both on the TP and in other regions of the world, which reflects the comprehensive effects of changes in temperature, soil moisture conditions and site-specific properties and can affect the decomposition of soil organic matter and greenhouse gas exchanges between the land surface and the atmosphere (Frauenfeld and Zhang, 2011; Peng et al., 2017).

Frozen ground can influence the eco-hydrological processes on the TP via runoff generation, groundwater-surface water interaction, soil moisture conditions as well as other means (Cheng and Wu, 2007; Jin et al., 2009; Yang et al., 2010; Wang et al., 2018b). Understanding the spatial pattern of frozen ground provides the basis for quantitatively assessing the eco-hydrological processes on the TP, which calls for more reliable frozen ground maps at finer resolution. In a changing climate, frozen ground changes can greatly affect the regional hydrology in the TP and water resources security in the downstream, where more than 1.4 billion people feed on the rivers originating from the TP (Immerzeel et al., 2010). The projections of future frozen ground changes can enable policy makers to develop appropriate strategies prior to the anticipated changes (Guo and Wang, 2016). Although there are already studies projecting global permafrost changes in the future (Slater and Lawrence, 2013; Guo and Wang, 2016), very limited studies focus on the TP (Lu et al., 2017) and the spatial resolution is not high enough for hydrological application. Therefore, more studies are needed to project the future frozen ground changes on the TP, including both permafrost and MTSFG changes at finer resolution.

Borehole observations provide solid information for mapping frozen ground distribution. However, they are hard to obtain, very expensive, and restricted to the point scale (Zhang et al., 2005; Frauenfeld and Zhang, 2011; Wu et al., 2015). Consequently, simple empirical models are developed to map the large scale permafrost and MTSFG distribution on the TP (Zhao et al., 2017). For example, Li and Cheng (1999) developed an elevation model to map permafrost distribution by determining the lower limit of permafrost; Nan et al. (2002) established a mean annual ground temperature (MAGT) model to determine the permafrost across the TP. These models, however, are established based on limited and unevenly distributed in-situ observations, and they are derived from the static variables which are hard to be used in future projections.

Meanwhile, semi-empirical models with simplified physical processes applicable to high-latitude permafrost were used for the frozen ground simulation on the TP, including the surface frost number model, temperature at top of permafrost (TTOP) model, Stefan model (Zou et al., 2017), etc. However, if the underlying assumptions of the models are not met, their spatial generalization ability needs to be carefully assessed (Walvoord and Kurylyk, 2016). Process-based models have also been applied to simulate frozen ground on the TP at larger scale, which considered both the thermal and hydrological processes, including CLM4 model (Guo et al., 2012), GIPL2 model (Qin et al., 2017a), GBEHM model (Qin et al., 2017b; Gao et al., 2018), Noah model (Wu et al., 2018), etc. Nevertheless, the process-based models still have limitations in describing the complicated cryospheric and eco-hydrological processes using explicit equations due to limited understanding of the cold region environment. They often make simplifications to certain physical processes, introduce plenty of parameters, and are usually computational intensive (Walvoord and Kurylyk, 2016).

Although in-situ observations like boreholes and testing pits are still rare on the TP, nowadays more and more spatial datasets including topography, temperature and soil properties are available with the assistance of new technologies like remote sensing. This makes the data-driven methods including statistics and machine learning methods potentially applicable in estimating the frozen ground on the TP (Li et al., 2011; Lary et al., 2016). The statistics and machine learning algorithms can be promising when the relationships between the explained and explanatory variables are hard to explicitly described, but they might also encounter problems like overfitting and underfitting (Domingos, 2012), and the performances of different algorithms might differ for a given problem hence need to be evaluated. The statistics and machine learning methods have been adopted in many fields of geoscience, and have also been introduced into cryospheric researches recently. Deluigi et al. (2017) used different statistics and machine learning algorithms to map the potential permafrost distribution in Western Swiss Alps. Shi et al. (2018) used the decision tree method to get the 1-km permafrost map on the TP. The performance of different categories of statistics and machine learning algorithms in frozen ground estimation on the TP, however, have never been evaluated and compared. Besides, these methods have not yet been applied to map the MTSFG distribution as well as the future frozen ground changes on the TP, which are important for the third pole region.

This study adopts statistics and machine learning algorithms to map the current and future frozen ground distribution, including permafrost and MTSFG on the TP. The objectives of this study are to (1) evaluate and compare the performances of different statistics and machine learning methods in frozen ground estimation on the TP; (2) generate high-resolution permafrost and MTSFG distribution maps on the TP; (3) project the response of frozen ground to the future climate change on the TP.

2. Methods

In this study, statistics and machine learning methods are adopted for two objectives: first, classification for mapping permafrost distribution, more specifically, whether permafrost exists in a certain grid on the Tibetan Plateau (TP); second, regression for predicting MTSFG distribution in non-permafrost region. This study selects logistic regression (LR), support vector machine (SVM) and random forest (RF) for classification. These algorithms are selected because they belong to three specific sub-domains of learning techniques, respectively linear parametric learning, non-parametric learning and ensemble learning (Deluigi et al., 2017). LR, despite its name, is only applicable for classification. Therefore, only SVM and RF are adopted and compared for regression. The three selected algorithms are introduced in supplementary material (see Text S1). Detailed procedures for addressing the two problems will be introduced in Sections 2.1 and 2.2.

2.1. Mapping the permafrost distribution

The entire Tibetan Plateau (TP) is classified into two frozen ground types: permafrost and non-permafrost regions in this study. All estimates exclude glaciers and lakes within the TP boundary. Different types of permafrost, i.e., continuous and discontinuous permafrost, are not distinguished. Seasonally frozen ground and unfrozen ground are both regarded as non-permafrost regions. The whole procedure for establishing the classification models and mapping the current and future permafrost distribution is illustrated as Fig. 1. Six variables that affect the thermal state of frozen ground are selected as the input for training the models: the mean annual air temperature (MAAT), the ratio of mean annual ground surface temperature to mean annual air

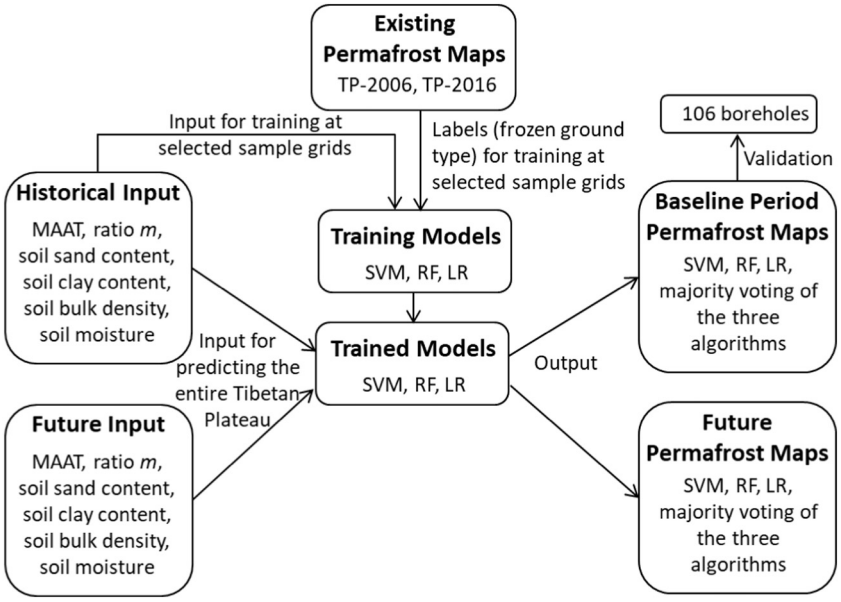
Existing Permafrost Maps
TP-2006, TP-2016
Input for training at selected sample grids
Labels (frozen ground type) for training at selected sample grids
106 boreholes
Validation
Historical Input
MAAT, ratio m, soil sand content, soil clay content, soil bulk density, soil moisture
Training Models
SVM, RF, LR
Baseline Period Permafrost Maps
SVM, RF, LR, majority voting of the three algorithms
Input for predicting the entire Tibetan Plateau
Trained Models
SVM, RF, LR
Output
Future Input
MAAT, ratio m, soil sand content, soil clay content, soil bulk density, soil moisture
Future Permafrost Maps
SVM, RF, LR, majority voting of the three algorithms

Fig. 1. Procedure diagram for establishing the classification models (permafrost distribution models) and mapping the current and future permafrost distribution.

temperature, soil bulk density, sand content, clay content and the mean annual soil moisture content.

To overcome the problem of inadequate borehole observations, this study adopts two existing permafrost maps, respectively TP-2006 and TP-2016 which will be further introduced in Section 3.2, to provide labels (frozen ground types) for training the models. There are differences between the two widely used maps (Fig. S1). The frozen ground types at the grids where the two maps agree (both permafrost and both non-permafrost regions) are more reliable and more likely to be stable in the recent decades. Therefore, we can develop models relating the frozen ground type and its influencing variables at these grids. Some of the grids with consistent frozen ground types in the two existing maps are selected as the training set for training the permafrost distribution models, which is introduced in supplementary material (see Text S2). Three permafrost maps can be generated from the trained models using LR, SVM and RF algorithm. These maps can be merged into one map using majority voting method: for each grid, if 2 or 3 of the 3 algorithms predict the presence of permafrost, then the grid is labeled as permafrost in the merged map, otherwise labeled as non-permafrost region. The newly generated permafrost maps are then validated by the borehole observations.

Using the models trained at the historical period, the future permafrost distribution can also be projected with the input at the future periods. We assume the ratio m and the soil properties not change in the future, then the ratio m, soil bulk density, sand content, clay content which are part of the input at the historical period are also adopted as the future period input. Besides, the MAAT and soil moisture in the future periods are adopted as input to predict the future permafrost distribution, which are derived from the air temperature and precipitation data of 5 General Circulation Models (GCMs), and these future data will be introduced in Section 3.5.

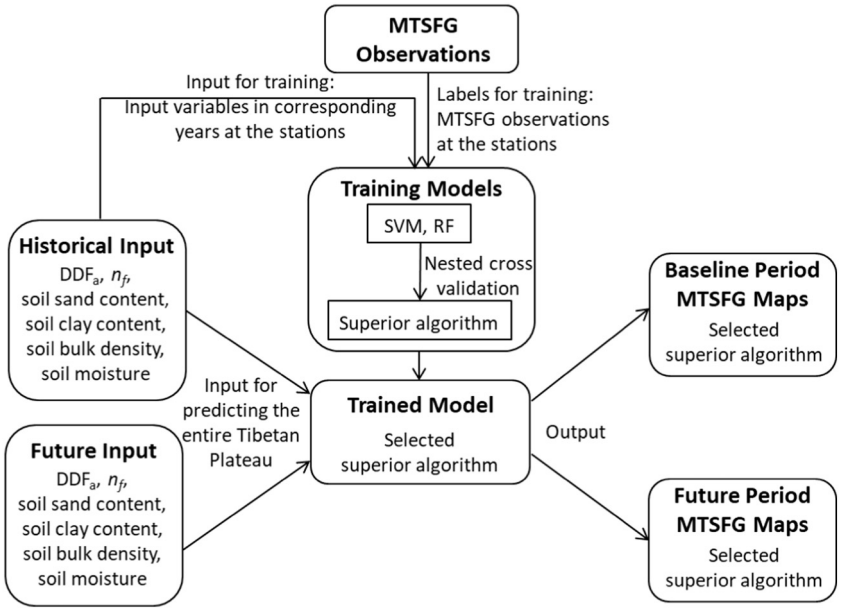
MTSFG Observations
Input for training:
Input variables in corresponding years at the stations
Labels for training:
MTSFG observations at the stations
Training Models
SVM, RF
Nested cross validation
Superior algorithm
Historical Input
DDF$_a$, n_f, soil sand content, soil clay content, soil bulk density, soil moisture
Baseline Period MTSFG Maps
Selected superior algorithm
Input for predicting the entire Tibetan Plateau
Trained Model
Selected superior algorithm
Output
Future Input
DDF$_a$, n_f, soil sand content, soil clay content, soil bulk density, soil moisture
Future Period MTSFG Maps
Selected superior algorithm

Fig. 2. Procedure diagram for establishing the regression model (MTSFG model) and mapping the current and future MTSFG distribution.

2.2. Mapping the maximum thickness of seasonally frozen ground (MTSFG)

The whole procedure for establishing the regression models and mapping the current and future MTSFG distribution is shown in Fig. 2. The value of MTSFG significantly correlates with the air freezing index (DDF_a) (Peng et al., 2017; Wang et al., 2018a). Six input variables influencing MTSFG are chosen for the regression problem, respectively the annual DDF_a, freezing n-factor (n_f), soil bulk density, sand content, clay content, and mean annual soil moisture content.

MTSFG observations are available at 94 meteorological stations on the TP during 1979–2014, which provide labels for training the models and will be further introduced in Section 3.4. A nested cross-validation method is adopted to evaluate and compare the spatial generalization ability of SVM and RF (Jung et al., 2011; Krstajic et al., 2014). First, we divide all the data into five parts with respect to elevation, since we want to obtain the MTSFG values at unknown sites with large elevation variations (Jung et al., 2011). Each time we select one part as the testing set, while the remaining four parts are used for tuning and training, and the model trained by the four parts is evaluated by the testing set. This procedure will be repeated for five times, hence each part of the data will serve as the testing set for once; afterwards the simulated results when serving as the testing set are aggregated and plotted versus the observed MTSFG to show the generalization ability of a certain model in predicting the MTSFG values at the unknown sites.

After cross-validation, MTSFG observations at all stations are used for tuning and training a new model using the selected algorithm with superior spatial generalization ability, and the trained model is used for predicting the current spatial distribution of MTSFG by adopting the input at the historical period mentioned above. We assume n_f and soil properties not change in the future, then n_f, soil bulk density, sand content, clay content which are part of historical period input are also adopted as future period input. Besides, future DDF_a and soil moisture are adopted as the future input, which are derived from the 5 GCMs and will be introduced in Section 3.5.

3. Data

3.1. Input data at the historical period

The air temperature data during 1979–2015 with 0.1° spatial resolution are from the China Meteorological Forcing Dataset developed by the Institute of Tibetan Plateau Research, Chinese Academy of Sciences (ITP/CAS) (He and Yang, 2011). In this study, air temperature are downscaled to 1-km resolution by adding an elevation adjustment term at each grid, which is calculated by multiplying the elevation difference (the difference between the elevation of the target 1-km resolution and the original 0.1° resolution) and the air temperature lapse rate (TLR) of a certain month. TLR reflects the rate of change in air temperature with increasing elevation. The values of TLR for different months are calculated by a linear regression method (X. Guo et al., 2016) based on the observations at the meteorological stations across the Tibetan Plateau (TP) (Table S2), and the mean annual TLR is −4.2 °C km^{-1}. Digital elevation data from the Shuttle Radar Topography Mission with a resolution of 90 m (Jarvis et al., 2008) are resampled to 1-km resolution as the target elevation. From the monthly air temperature, we can derive the mean annual air temperature (MAAT) and the air freezing index (DDF_a). DDF_a is calculated by summing all the daily mean air temperature below 0 °C in a freezing year which is defined as the period between July of one year and June of the following year (Frauenfeld et al., 2007).

The thermal state of frozen ground is directly impacted by ground temperature rather than the air temperature. The ratio of mean annual ground surface temperature to mean annual air temperature (hereafter ratio m) and freezing n-factor (n_f) represent the energy balance between the ground surface and the near-surface atmosphere, and n_f is defined as the ratio of ground surface freezing index to air freezing index (DDF_a) (Klene et al., 2001). The Moderate Resolution Imaging Spectroradiometer (MODIS) provide the 1-km Land Surface Temperature (LST) data since 2003 (Wan, 2007). This study adopts the following formula to obtain the daily mean ground surface temperature from different MODIS LST observations (Zou et al., 2017):

$$GST = 0.180 \times Terra_{day} + 0.269 \times Terra_{night} + 0.143 \times Aqua_{day} + 0.435 \times Aqua_{night} + 0.896, \quad (1)$$

where GST is the daily mean ground surface temperature; $Terra_{day}$, $Terra_{night}$, $Aqua_{day}$, and $Aqua_{night}$ are respectively the MOD11A2 (Terra MODIS) and MYD11A2 (Aqua MODIS) daytime/nighttime LST products. Then the mean annual ground surface temperature be derived, and the ground surface freezing index can be calculated by summing all the daily mean ground surface temperature below 0 °C in a freezing year. We select the overlapped period of air temperature data from ITP/CAS and the MODIS LST data, 2003–2010, as the baseline period to represent the current state of the frozen ground on the TP. The spatial distribution of the mean values of ratio m and n_f during the baseline period (2003–2010) is shown as Fig. S6.

The soil bulk density, sand content and clay content from the Soil Database of China for Land Surface Modeling (http://globalchange.bnu.edu.cn/research/soil2) are adopted by this study (Shangguan et al., 2013). This study adopts the weighted mean value of the top seven layers to the depth of 1.383 m. The 0–100 cm depth soil moisture data from the China Soil Moisture Dataset from Microwave Data Assimilation (CSMDA) (http://en.tpedatabase.cn) are adopted by this study (Yang et al., 2016). This dataset assimilates passive microwave data (AMSR-E TB) through a Dual-Pass Microwave Land Data Assimilation System and was validated to have ±5% volumetric water content accuracy for the TP (Yang et al., 2016).

3.2. Data providing labels for training the permafrost distribution models

This study selects two existing permafrost maps to provide labels (frozen ground type) for training the permafrost distribution models as mentioned in Section 2.1 (Fig. S1). The first map is *the 1:4,000,000 Map of Glaciers, Frozen Ground and Deserts in China*, compiled by the Cold and Arid Regions Environmental and Engineering Research Institute, Chinese Academy of Sciences (hereafter TP-2006) (Wang et al., 2006) (Fig. S1a). In this map, permafrost distribution was generated using a 0.5 °C mean annual ground temperature (MAGT) isotherm as the threshold. The MAGT across TP was interpolated based on the linear relationship between observed MAGT and the elevation, latitude at 76 boreholes along the Qinghai–Xizang Highway (Nan et al., 2002). The second map is derived from TTOP model combining both MODIS LST data and ground observation datasets (hereafter TP-2016) (Zou et al., 2017) (Fig. S1b). These two maps are resampled to 1-km resolution. The spatial differences between the two maps are compared (Fig. S1c). Some of the grids where the two existing maps agree in frozen ground types are selected to form the training set for training the permafrost distribution models (see Text S2).

3.3. Data for validating generated permafrost maps

This study collects 106 boreholes providing frozen ground type information at different regions of TP (Fig. 3 and Table S3), including West Kunlun in northwestern TP (Chen et al., 2015), Gaize in interior TP (Chen et al., 2016), source region of the Yellow River in northeastern TP (Luo et al., 2012), Qinghai-Tibetan Highway (G109) in central TP as well as other region across the TP (Qin et al., 2017a). The drilling time of these boreholes are 2009–2012 which are within or close to the baseline period (2003–2010) adopted in this study, thus can be used for validating the baseline period permafrost maps generated by this study.

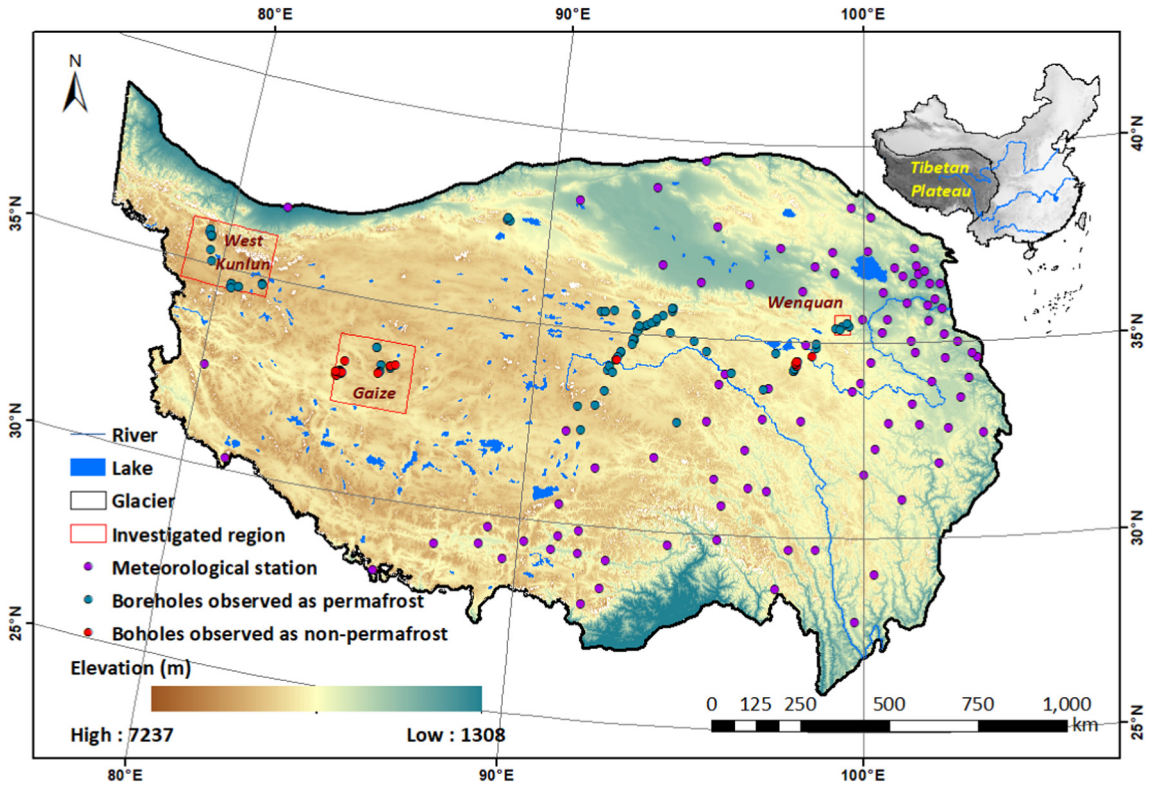

Fig. 3. Study area and locations of the 106 boreholes, 94 meteorological stations and the three investigated regions.

3.4. Frozen soil depth observations for MTSFG distribution

The frozen soil depth observations at the meteorological stations on the TP since 1979 are provided by the China Meteorological Administration for estimating the MTSFG distribution as mentioned in Section 2.2. The daily frozen depth is manually measured by the standard frozen soil apparatus (CMA, 2007). The apparatus is vertically buried in the meteorological field, and the frozen depth is measured by the length of ice in the inner rubber tube. This study selects 94 meteorological stations with consecutive frozen soil depth observations for more than 10 years on the TP (Fig. 3). MTSFG is the maximum depth from the ground surface to the freezing front in a freezing season, and we use the maximum observed daily frozen depth in a freezing year starting from July as the value of MTSFG at a certain station.

3.5. Input data at the future period

As mentioned in Sections 2.1 and 2.2, future MAAT, DDF_a and soil moisture are adopted as part of input to predict the future permafrost and MTSFG distribution. This study adopts the monthly air temperature and precipitation data from 5 GCMs, respectively NorESM1-M, MIROC-ESM-CHEM, IPSL-CM5A-LR, HadGEM2-ES and GFDL-ESM2M during the Coupled Model Intercomparison Project Phase 5 experiment (Taylor et al., 2012). The raw climate outputs from the 5 GCMs have been corrected by a statistical bias correction method (Hempel et al., 2013) according to the Inter-Sectoral Impact Model Intercomparison Project (ISI-MIP) simulation protocol (https://esg.pik-potsdam.de/search/isimip/) (Warszawski et al., 2014).

We obtain the air temperature and precipitation data during the baseline period and future periods including 2041–2050 (2040s) and 2091–2099 (2090s) under Representative Concentration Pathway (RCP) 4.5 scenario. Delta method is adopted to project the future air temperature and precipitation (Su et al., 2016) and derive the future soil moisture. Details can be found in supplementary material (see Text S3).

4. Results

4.1. Permafrost distribution: validation by borehole observations

The generated permafrost maps are validated by the 106 boreholes across the TP and the accuracies are also compared with TP-2016 (Table 1). In respect with the 90 boreholes observed as permafrost, LR, RF and SVM has prediction accuracy of 97.8%, 96.7% and 94.4%, and the former two are slightly better than TP-2016 (95.6%). As for the 16 boreholes observed with no permafrost, LR and SVM perform better than RF with the accuracy of 43.8%, slightly lower than TP-2016 (56.3%). LR has the best overall accuracy of 89.6% for all boreholes among the three algorithms, which equals the accuracy of TP-2016 (83.0%). The map derived from majority voting results of the three individual algorithms has an overall accuracy of 89.6%, which is the same as the best performed individual algorithm LR and TP-2016. The results

Table 1
Accuracy evaluation of the existing and generated permafrost maps based on the 106 boreholes.

	TP-2016	LR	SVM	RF	Voting
PP	86	88	85	87	88
PN	4	2	5	3	2
NP	7	9	9	10	9
NN	9	7	7	6	7
Permafrost accuracy	95.6%	97.8%	94.4%	96.7%	97.8%
Non-permafrost accuracy	56.3%	43.8%	43.8%	37.5%	43.8%
Total accuracy	89.6%	89.6%	86.8%	87.7%	89.6%

Note: PP = permafrost observed by borehole and correctly identified as permafrost by the permafrost map, PN = permafrost observed by borehole but identified as non-permafrost region by the permafrost map, NP = non-permafrost region observed by borehole but identified as permafrost by the permafrost map, NN = non-permafrost region observed by borehole and correctly identified as non-permafrost region by the permafrost map.

indicate that according to the 106 borehole observations, the permafrost maps derived from LR and the majority voting of the three algorithms can reach at least the same accuracy as TP-2016. Therefore, the statistics and machine learning methods adopted in this study are applicable in mapping the permafrost distribution across the TP. The generated maps are also compared with the survey-based maps at three investigated regions in the Supplementary material (see Text S4).

4.2. MTSFG distribution: nested cross validation

Nested cross-validation is adopted as mentioned in Section 2.2 to compare the spatial generalization ability of SVM and RF. Comparing the performances of the testing set derived from SVM (Fig. S7a) and RF (Fig. S7b) when partitioning the data by elevation, the correlation coefficient (r) and rooted mean squared error ($RMSE$) of SVM ($r = 0.84$, $RMSE = 34.39$ cm) are better than those of RF ($r = 0.79$, $RMSE = 38.04$ cm). The RF results significantly underestimate the MTSFG values at higher elevation with deeper MSTFG. Therefore, SVM is superior in spatial generalization ability thus more suitable for predicting MTSFG at unknown sites even with higher elevation on the TP. Consequently, only SVM algorithm is selected for mapping the MTSFG distribution. We also evaluate the temporal generalization ability of SVM by repeating the nested cross-validation procedure but changing the partitioning criterion from elevation to time (Jung et al., 2011) (Fig. S7c). The results ($r = 0.94$, $RMSE = 22.07$ cm) show that SVM also has good temporal generalization ability thus can be used to project the MTSFG distribution in the future.

4.3. Current permafrost distribution and future changes

Three permafrost maps at the baseline period can be obtained by LR, SVM and RF (Fig. S8), and a merged map is also derived by majority voting of the three individual algorithms (Fig. 4). Among the three algorithms, LR predicts the largest permafrost area of 1,180,952 km^2 (46.2% of the TP), while RF predicts the smallest permafrost area of 1,143,019 km^2 (44.7% of the TP) (Table S4). The differences in permafrost area percentages between the maps derived from the 3 algorithms are very small (around 1.5% area of the TP). The majority voting results of the three algorithms predict 45.9% area of the TP underlain by permafrost, while the remaining 54.1% area is classified as non-permafrost regions (Table S4).

The permafrost distribution in the future can be projected by the 5 GCMs under RCP 4.5 scenario, and only the majority voting results of the three algorithms are displayed and analyzed from this paragraph on due to the article length limitation. The projected permafrost degradation rates vary with GCMs (Table S5). GFDL-ESM2M projects the mildest permafrost degradation: there will still be respectively 37.1% and 33.3% area of the TP underlain by permafrost in the 2040s and the 2090s, indicating 16.5% and 25.1% of the permafrost in the baseline period will disappear by the 2040s and the 2090s. MIROC-ESM-CHEM projects the most dramatic permafrost degradation: there will be only 26.5% and 16.5% area of the TP underlain by permafrost in the 2040s and the 2090s, indicating 40.3% and 62.9% of the current permafrost will disappear by the 2040s and the 2090s (Table S5). There will be 32.9% and 24.9% area of the TP underlain by permafrost in the 2040s and the 2090s by the mean of the projections from the 5 GCMs, indicating 25.9% and 43.9% of the current permafrost will disappear by the 2040s and the 2090s (Table S5).

The permafrost degradation and non-permafrost region expansion processes from the baseline period to the 2040s and 2090s projected by the 5 GCMs are shown in Fig. 5. The green area shows the region which is underlain by permafrost in the baseline period but will degrade into non-permafrost regions by the 2040s; while the red area shows where the permafrost degradation is projected to occur from the 2040s to the 2090s (Fig. 5). It can be seen that the potential permafrost degradation is more likely to occur at the outer perimeter of permafrost on the southwestern and eastern TP as well as the interior TP (Fig. 5).

The permafrost and non-permafrost area distribution along elevation in the baseline period and in the future can be seen in Fig. S9. The permafrost area decreases and non-permafrost area increases are projected to occur at almost all elevation intervals above 3000 m from baseline period to the 2040s and 2090s, and the most dramatic permafrost degradation is likely to occur in 4200–5400 m (Fig. S9). At this elevation range, the permafrost area is projected to decrease from the current 946,851 km^2 to 513,338 km^2 in the 2090s by the mean of the projections from the 5 GCMs, and more than 80% of the permafrost area decreases are projected to concentrate at this elevation range. In the baseline period, 24.1% area of all the permafrost on the TP is distributed below 4600 m, while this percentage is projected to fall to 19.7% and 16.2% in the 2040s and 2090s projected by the mean of the projections from the 5 GCMs, indicating the upshifting of permafrost lower limit in the future.

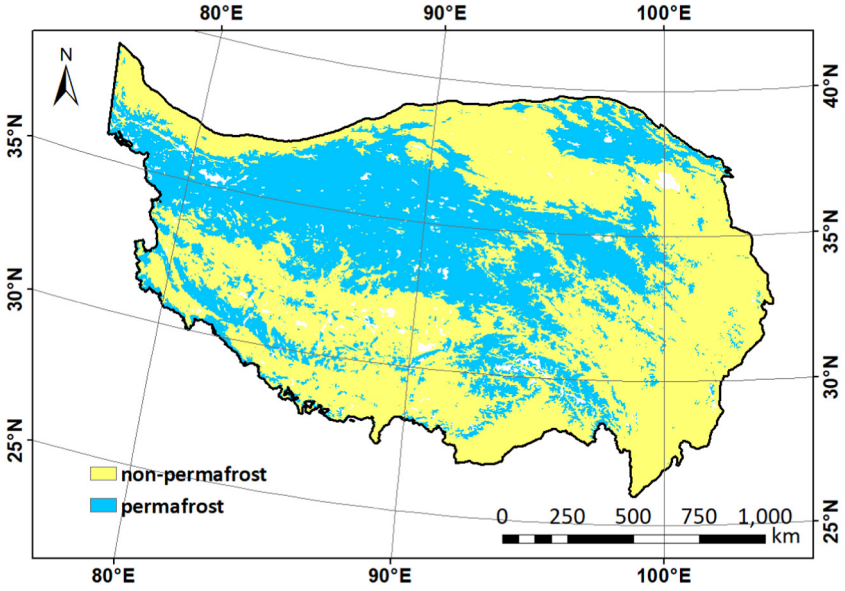

Fig. 4. Permafrost distribution in the baseline period on the TP derived from the majority voting results of LR, SVM and RF.

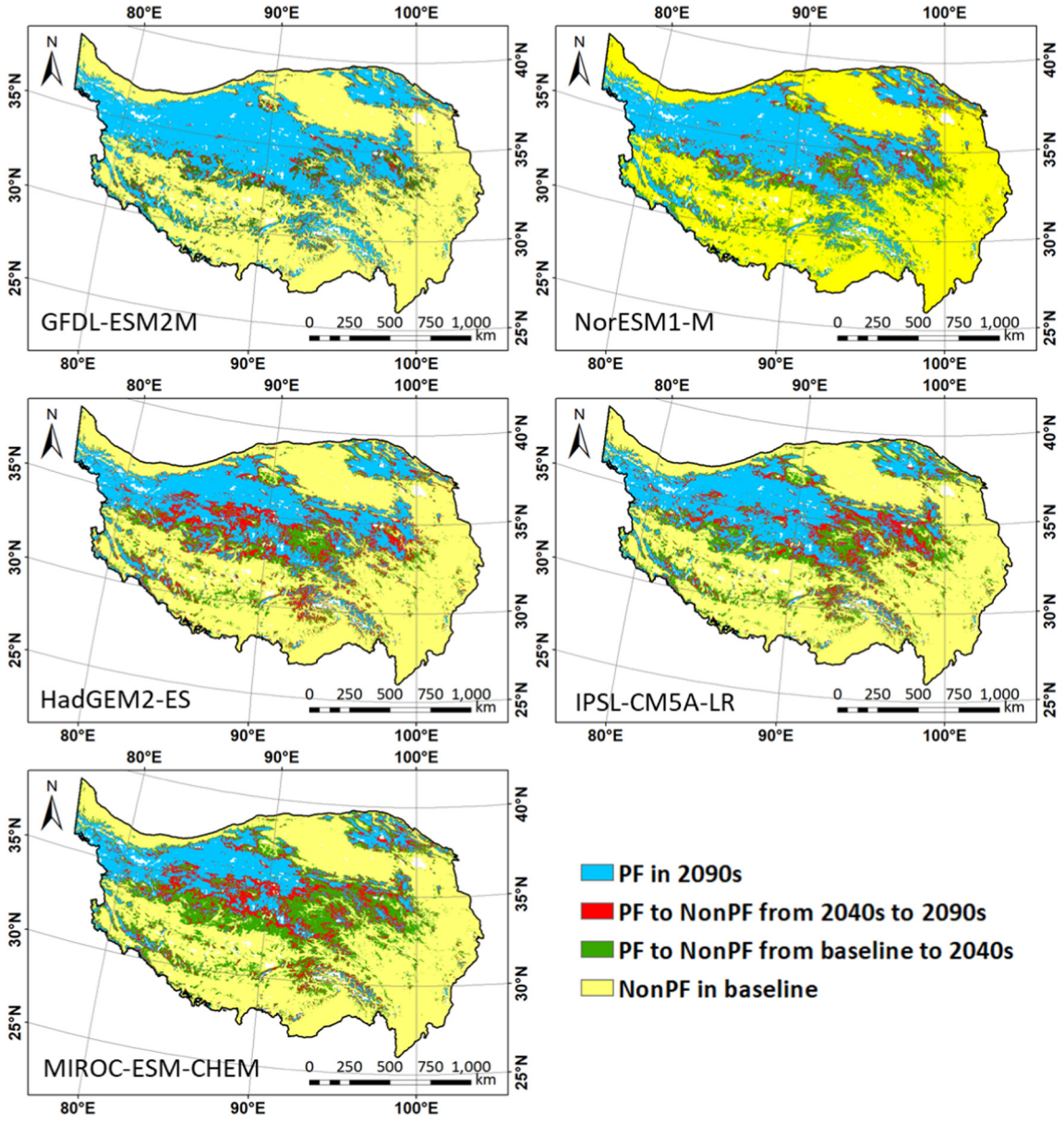

Fig. 5. Permafrost degradation and non-permafrost region expansion processes from the baseline period to the 2040s and 2090s projected by the 5 GCMs from the majority voting results of LR, SVM and RF.

4.4. Current MTSFG distribution and future changes

SVM is adopted to estimate the current and future MTSFG distribution over the TP as mentioned in Section 4.2. The value of MTSFG is physically meaningful only in non-permafrost regions, so we use the spatial extent of non-permafrost regions from the permafrost distribution map derived from the majority voting of the three algorithms (Fig. 4), and use this fixed extent to analyze the MTSFG changes in the future compared with the baseline period. The spatial distribution of MTSFG on the TP in the baseline period can be seen in Fig. 6. The MTSFG is shallower than 25 cm in the southern and southeastern TP where the elevation is relatively low. The largest values of MTSFG occur in the permafrost/non-permafrost transitional margins where the MTSFG can even exceed 300 cm (Fig. 6).

The MTSFG distribution in the 2040s and 2090s can be projected by the 5 GCMs under RCP 4.5 scenario using SVM. Different rates of MTSFG decreases are projected by the 5 GCMs, and their spatial distribution is shown in Fig. 7. Among the 5 GCMs, MIROC-ESM-CHEM projects the most dramatic MTSFG decreases: the decrease in MTSFG at almost all the southwestern TP is projected to exceed 50 cm in the 2090s compared with the baseline period (Fig. 7). All the 5 GCMs project an elevation-dependent MTSFG degradation on the TP, indicating the MTSFG decrease is larger at higher elevation compared with the decrease at lower elevation (Fig. S10).

5. Discussion

5.1. Permafrost distribution compared with previous studies

This study aims at testing the applicability of statistics and machine learning algorithms in predicting permafrost distribution. According to the overall accuracy for all the boreholes, the permafrost maps derived from LR and the majority voting of the three algorithms can reach the same accuracy as TP-2016 (Table 1), which gives us more confidence in using statistics and machine learning methods for mapping the spatial pattern and projecting the future changes of permafrost, since TP-2016 was the validated to have better ability in recognizing permafrost boundary than previous permafrost maps on the TP (Zou et al., 2017).

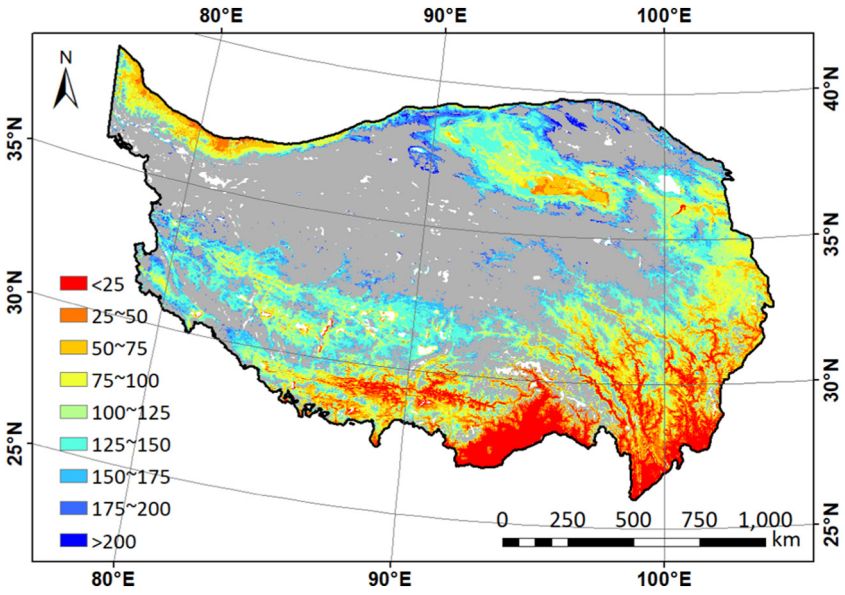

Fig. 6. Spatial distribution of MTSFG (unit: cm) in the baseline period on the TP derived from SVM.

The maps derived by this study are not necessarily more accurate than TP-2016, but at least provide different approaches to predict permafrost distribution.

Many previous studies also estimated the permafrost area on the TP based on different methods, including the elevation model (Zhao et al., 2017), MAGT model (Wang et al., 2006), TTOP model (Zou et al., 2017), process-based model (Wu et al., 2018), decision tree model (Shi et al., 2018), and other methods (Xu et al., 2016; Ran et al., 2018). In order to eliminate the effects of permafrost degradation over time, only the permafrost maps derived from recent data close to the baseline period of this study (2003–2010) are selected for comparison. Different permafrost areas were predicted by the previous studies as shown in Table S6, and the permafrost area derived from this study is very close to the estimates from the MAGT, Noah and the decision tree models (Table S6).

5.2. Future permafrost changes compared with previous studies

The five GCMs adopted in this study are obtained from the ISI-MIP project as introduced in Section 3.5. These GCMs are selected by the ISI-MIP project since they span the space of global mean temperature change and relative precipitation changes as best as possible (Warszawski et al., 2014). The soil temperature simulations in GCMs are usually not directly adopted for predicting permafrost distribution due to simplification in land surface schemes and coarse resolution (Slater and Lawrence, 2013). Instead, the outputs of GCMs are usually bias-corrected, downscaled and adopted as the input of permafrost models to indirectly project the future permafrost distribution. The bias-corrected GCM data from ISI-MIP capture the spatial patterns of climatic variables very well in the upper Yangtze River basin located on the TP (Su et al., 2017), and have been applied in projecting the future changes in frozen ground on the TP by previous studies (Lu et al., 2017; Wang et al., 2018a). Furthermore, this study uses the temperature lapse rate to downscale the air temperature to 1 km.

Some projections have been employed on the TP. Lu et al. (2017) adopted the same 5 GCMs from ISI-MIP as our study adopts, and used Surface Frost Number model to predict permafrost distribution with the Lund-Potsdam-Jena model simulated 20 cm depth ground temperature as input. They projected that 18%, 33% and 44% of the current permafrost will disappear in the near-term (2011–2040), mid-term (2041–2070) and long-term (2071–2099) future by the mean of the projections from the 5 GCMs under RCP 4.5 scenario. In comparison, approximately 26% and 44% of the current permafrost is projected to disappear by the 2040s and the 2090s under RCP 4.5 scenario on the TP by the mean of projections from the 5 GCMs in this study (Table S5), which are similar to the projections of Lu et al. (2017). This study generates the permafrost maps with finer resolution (1 km) by downscaling air temperature with TLR than the 0.5° resolution maps Lu et al. (2017) derived. Guo and Wang (2016) projected around 67% of current permafrost on the TP would disappear by 2080–2099 under RCP 4.5 scenario using the surface frozen index model, which is higher than the degradation rates we project. The permafrost area percentages decreases on the TP derived from this study are quite similar to the values in the Northern Hemisphere projected by Lawrence et al. (2012), and they estimated that around 28% and 49% of the current permafrost are projected to disappear by the middle and the end of the 21st century under RCP 4.5 scenario.

5.3. MTSFG distribution and elevation-dependent degradation

This study compares the spatial generalization ability for mapping MTSFG between SVM and RF through nested cross validation, and select SVM algorithm to map the spatial distribution and future changes of MTSFG (Fig. S7). Peng et al. (2017) mapped the MTSFG distribution across China using semi-empirical Stefan equation. They used the observational MTSFG and DDF_a at the meteorological station to calculate a lumped edaphic parameter E for each station, and then interpolated the parameter E to the regional scale using Kriging and calculated the spatial distribution of MTSFG using the distributed DDF_a. In contrast, the spatial distribution of the input variables in this study are relatively more physically-based, including the distributed temperature and soil datasets, as well as n_f representing the energy balance between the ground surface and the near-surface atmosphere.

Elevation-dependent MTSFG degradation is projected on the TP, which means the MTSFG decrease is more dramatic at higher elevation compared with the decrease at lower elevation (Fig. S10). We examine the MTSFG decrease trend during 1979–2014 using the MTSFG observations at the 94 meteorological stations on the TP. The results show that the elevation-dependent MTSFG degradation exists in the historical

Fig. 7. Spatial distribution of the change in MTSFG (cm) of the (a) 2040s and (b) 2090s in respect to the baseline period (2003–2010) projected by 5 GCMs under RCP 4.5 scenario using SVM.

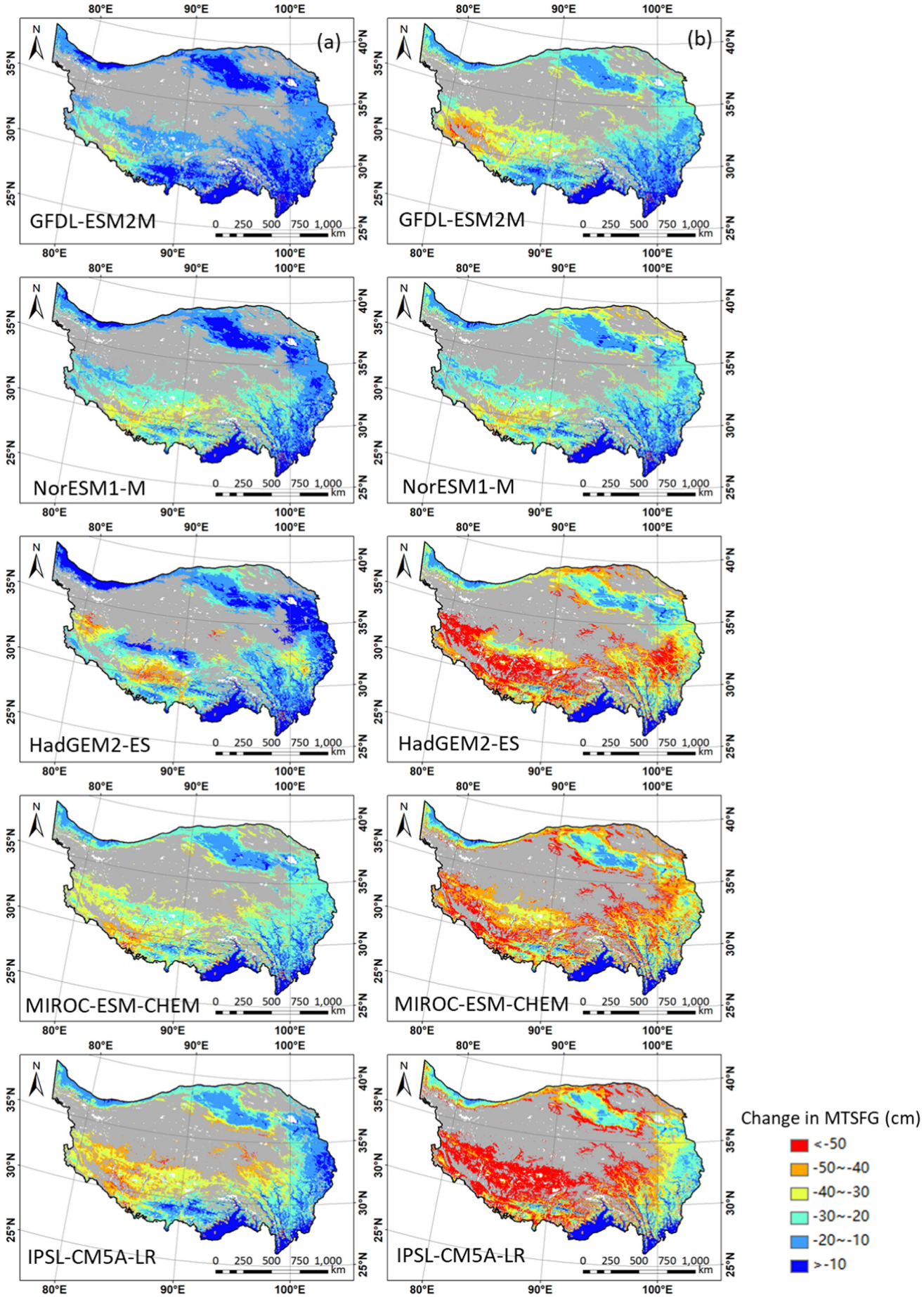
(a)
(b)
GFDL-ESM2M
NorESM1-M
HadGEM2-ES
MIROC-ESM-CHEM
IPSL-CM5A-LR
80°E
90°E
100°E
40°N
35°N
30°N
25°N
N
0 250 500 750 1,000 km
Change in MTSFG (cm)
<-50
-50~-40
-40~-30
-30~-20
-20~-10
>-10

period (Fig. S11), therefore learned by SVM in this study. This phenomenon can result from the elevation dependent air temperature warming. The higher elevation experiences larger air temperature increase in the future, indicating the elevation-dependent warming is projected to occur on the TP as projected by the 5 GCMs (Fig. S12), which is consistent with the results from D. Guo et al. (2016). The air temperature in cold season increases more rapidly than warm season on the TP as found by Su et al. (2016), which exaggerates the elevation-dependent degradation, since MTSFG is mainly control by the cold season temperature. Besides, the soil moisture condition discrepancy might also contribute to the elevation-dependent MTSFG degradation. The western TP tends to have higher elevation as well as lower soil moisture content as indicated by the precipitation and soil moisture distribution on the TP (Fig. S13). With the same input energy decrease, the MTSFG at drier soil tends to decrease more than wetter soil (Wang et al., 2018a).

5.4. Factors affecting the spatial pattern and potential changes of frozen ground

In this study, we adopt three categories of factors in predicting the spatial pattern of frozen ground, respectively the atmospheric forcing indicated by MAAT and DDF_a, the soil properties indicated by soil bulk density, texture and soil moisture content, and the land surface factors between the near-surface atmosphere and the ground, indicated by the ratio m and n_f. The spatial distribution ratio m and n_f reflect the comprehensive effects of vegetation, snow cover and other land surface factors with the assistance of remote sensing based MODIS LST. It can be seen that the areas with lower ratio m are consistent with the areas with denser vegetation indicated by larger mean annual leaf area index derived from the 3rd generation of Normalized Difference Vegetation Index of the Global Inventory Modeling and Mapping Studies (Zhu et al., 2013) (Figs. S6 and S14).

When projecting the future changes of frozen ground, we only consider the changes of air temperature and soil moisture condition as the causes of potential changes, and assume the ratio m and n_f not change over time. We calculate the trend significance of ratio m and n_f on the TP based on the annual observed values during 2003–2016 by Mann-Kendall nonparametric test method (Wang et al., 2018a), and find non-significant trends of the two ratios at 0.05 significance level at most areas of TP (Fig. S15), indicating our assumption is reasonable at most areas on the TP during 2003–2016. If the ground surface temperature increases more rapidly than the air temperature as observed at several stations in the source region of the Yellow River (Wang et al., 2018a), m may increase and n_f may decrease in the future, resulting in more dramatic frozen ground degradation relative to the predicted estimates in this study. Besides, the geological structure, the upward thermal flux and the micro-topography within the 1-km grid are not considered due to data availability in this study, which might cause uncertainties in our generated maps, and can be improved in future studies.

6. Conclusions

This study estimates the permafrost and MTSFG distribution in the baseline period (2003–2010) and in the future (2040s and 2090s) using statistics and machine learning algorithms. LR, SVM and RF are adopted to generate the permafrost maps on the TP and validated by borehole observations. The performances of SVM and RF for mapping the MTSFG distribution are also compared by nested cross validation method. According to the results, the following conclusions have been reached:

1) LR, SVM and RF are all capable of mapping permafrost distribution on the TP. According to the 106 borehole observations, the map derived from LR performs better than the other two algorithms with an overall accuracy of 89.6%, which is the same as the existing map TP-2016.
2) According to the majority voting results of the three algorithms, 45.9% area of the TP is underlain by permafrost in the baseline period, while the remaining 54.1% area is classified as non-permafrost region. There will be 32.9% and 24.9% area of the TP underlain by permafrost in the 2040s and the 2090s by the mean of the projections from the 5 GCMs under RCP 4.5 scenario, indicating 25.9% and 43.9% of current permafrost will disappear by the 2040s and the 2090s.
3) SVM is superior in spatial generalization than RF when mapping the MTSFG distribution according to the nested cross validation results, therefore only SVM is selected for mapping the MTSFG distribution on the TP.
4) According to the results by SVM, MTSFG values generally decrease from the west to the east. The most dramatic decrease in MTSFG (over 50 cm) will occur in the southwestern TP in the 2090s compared with the baseline period. An elevation-dependent MTSFG degradation on the TP is projected in the future, which means the MTSFG decrease is projected to be larger at higher elevation compared with the decrease at lower elevation.

This study introduces the statistics and machine learning algorithms to the cryospheric field and provides alternative approaches to map the spatial distribution and potential changes of frozen ground on the TP with a relatively high resolution. The maps derived by this study can also serve as benchmarks for simulations on the TP which can export permafrost distribution and frozen depth as intermediate or final variables. Since 25.9% and 43.9% of current permafrost on the TP is projected to disappear by the 2040s and the 2090s estimated by this study, the future responses of streamflow and vegetation to frozen ground degradation are needed to be evaluated by the future studies.

Acknowledgements

This research was supported by the National Natural Science Foundation of China (Grant No. 41630856 and 91425303) and the Strategic Priority Research Program of Chinese Academy of Sciences, Grant No. XDA20100103. The authors thank the editor and four anonymous reviewers for their constructive and detailed comments.

Appendix A. Supplementary data

Supplementary data to this article can be found online at https://doi.org/10.1016/j.scitotenv.2018.08.369.

References

Chen, H., et al., 2015. Noah modelling of the permafrost distribution and characteristics in the West Kunlun Area, Qinghai-Tibet Plateau, China. Permafr. Periglac. Process. 26 (2), 160–174.
Chen, J., et al., 2016. Some characteristics of permafrost and its distribution in the Gaize Area on the Qinghai—Tibet Plateau, China. Arct. Antarct. Alp. Res. 48 (2), 395–409.
Cheng, G., Wu, T., 2007. Responses of permafrost to climate change and their environmental significance, Qinghai-Tibet Plateau. J. Geophys. Res. Earth Surf. 112 (F2).
CMA, 2007. Part 14: measurement of frozen soil. Specifications for Surface Meteorological Observation. China Meteorological Press, Beijing, China (in Chinese).
Cuo, L., et al., 2015. Frozen soil degradation and its effects on surface hydrology in the northern Tibetan Plateau. J. Geophys. Res. Atmos. 120 (16), 8276–8298.
Deluigi, N., Lambiel, C., Kanevski, M., 2017. Data-driven mapping of the potential mountain permafrost distribution. Sci. Total Environ. 590, 370–380.
Domingos, P., 2012. A few useful things to know about machine learning. Commun. ACM 55 (10), 78–87.
Frauenfeld, O.W., Zhang, T.J., 2011. An observational 71-year history of seasonally frozen ground changes in the Eurasian high latitudes. Environ. Res. Lett. 6 (4), 044024.
Frauenfeld, O.W., Zhang, T.J., McCreight, J.L., 2007. Northern hemisphere freezing/thawing index variations over the twentieth century. Int. J. Climatol. 27 (1), 47–63.
Gao, B., et al., 2018. Change in frozen soils and its effect on regional hydrology, upper Heihe basin, northeastern Qinghai–Tibetan Plateau. Cryosphere 12 (2), 657–673.
Gruber, S., 2012. Derivation and analysis of a high-resolution estimate of global permafrost zonation. Cryosphere 6 (1), 221.
Guo, D., Wang, H., 2016. CMIP5 permafrost degradation projection: a comparison among different regions. J. Geophys. Res. Atmos. 121 (9), 4499–4517.

Guo, D., Wang, H., Li, D., 2012. A projection of permafrost degradation on the Tibetan Plateau during the 21st century. J. Geophys. Res. Atmos. 117 (D5).
Guo, D., Yu, E., Wang, H., 2016. Will the Tibetan Plateau warming depend on elevation in the future? J. Geophys. Res. Atmos. 121 (8), 3969–3978.
Guo, X., Wang, L., Tian, L., 2016. Spatio-temporal variability of vertical gradients of major meteorological observations around the Tibetan Plateau. Int. J. Climatol. 36 (4), 1901–1916.
He, J., Yang, K., 2011. China Meteorological Forcing Dataset. Cold and Arid Regions Science Data Center at Lanzhou.
Hempel, S., Frieler, K., Warszawski, L., Schewe, J., Piontek, F., 2013. A trend-preserving bias correction–the ISI-MIP approach. Earth Syst. Dynam. 4 (2), 219–236.
Immerzeel, W.W., van Beek, L.P.H., Bierkens, M.F.P., 2010. Climate change will affect the Asian water towers. Science 328 (5984), 1382–1385.
Jarvis, A., Reuter, H.I., Nelson, A., Guevara, E., 2008. Hole-filled Seamless SRTM Data V4. International Centre for Tropical Agriculture (CIAT).
Jin, H.J., et al., 2009. Changes in frozen ground in the Source Area of the Yellow River on the Qinghai-Tibet Plateau, China, and their eco-environmental impacts. Environ. Res. Lett. 4 (4).
Jung, M., et al., 2011. Global patterns of land-atmosphere fluxes of carbon dioxide, latent heat, and sensible heat derived from eddy covariance, satellite, and meteorological observations. J. Geophys. Res. Biogeosci. 116 (G3).
Klene, A.E., Nelson, F.E., Shiklomanov, N.I., Hinkel, K.M., 2001. The n-factor in natural landscapes: variability of air and soil-surface temperatures, Kuparuk River basin, Alaska, USA. Arct. Antarct. Alp. Res. 33 (2), 140–148.
Krstajic, D., Buturovic, L.J., Leahy, D.E., Thomas, S., 2014. Cross-validation pitfalls when selecting and assessing regression and classification models. J. Cheminform. 6 (1), 10.
Lary, D.J., Alavi, A.H., Gandomi, A.H., Walker, A.L., 2016. Machine learning in geosciences and remote sensing. Geosci. Front. 7 (1), 3–10.
Lawrence, D.M., Slater, A.G., Swenson, S.C., 2012. Simulation of present-day and future permafrost and seasonally frozen ground conditions in CCSM4. J. Clim. 25 (7), 2207–2225.
Li, X., Cheng, G., 1999. A GIS-aided response model of high-altitude permafrost to global change. Sci. China Ser. D Earth Sci. 42 (1), 72–79.
Li, X., et al., 2008. Cryospheric change in China. Glob. Planet. Chang. 62 (3), 210–218.
Li, J., Heap, A.D., Potter, A., Daniell, J.J., 2011. Application of machine learning methods to spatial interpolation of environmental variables. Environ. Model. Softw. 26 (12), 1647–1659.
Lu, Q., Zhao, D., Wu, S., 2017. Simulated responses of permafrost distribution to climate change on the Qinghai–Tibet Plateau. Sci. Rep. 7 (1), 3845.
Luo, D., et al., 2012. New progress on permafrost temperature and thickness in the source area of the Huanghe River. Sci. Geogr. Sin. 32 (7), 898–904 (in Chinese).
Luo, D.L., et al., 2016. Recent changes in the active layer thickness across the northern hemisphere. Environ. Earth Sci. 75 (7), 1–15.
Nan, Z.T., Li, S.X., Liu, Y.Z., 2002. Mean annual ground temperature distribution on the Tibetan Plateau: permafrost distribution mapping and further application. J. Glaciol. Geocryol. 24 (2), 142–148 (in Chinese).
Peng, X., et al., 2017. Response of seasonal soil freeze depth to climate change across China. Cryosphere 11 (3), 1059.
Qin, Y., et al., 2017a. Numerical modeling of the active layer thickness and permafrost thermal state across Qinghai-Tibetan Plateau. J. Geophys. Res. Atmos. 122 (21).
Qin, Y., et al., 2017b. Impacts of climate warming on the frozen ground and eco-hydrology in the Yellow River source region, China. Sci. Total Environ. 605, 830–841.
Qiu, J., 2008. China: the third pole. Nature 454 (7203), 393–396.
Ran, Y., Li, X., Cheng, G., 2018. Climate warming over the past half century has led to thermal degradation of permafrost on the Qinghai–Tibet Plateau. Cryosphere 12 (2), 595–608.
Shangguan, W., et al., 2013. A China data set of soil properties for land surface modeling. J. Adv. Model. Earth Syst. 5 (2), 212–224.
Shi, Y., et al., 2018. Permafrost presence/absence mapping of the Qinghai-Tibet Plateau based on multi-source remote sensing data. Remote Sens. 10 (2), 309.
Slater, A.G., Lawrence, D.M., 2013. Diagnosing present and future permafrost from climate models. J. Clim. 26 (15), 5608–5623.
Su, F., et al., 2016. Hydrological response to future climate changes for the major upstream river basins in the Tibetan Plateau. Glob. Planet. Chang. 136, 82–95.
Su, B., Huang, J., Zeng, X., Gao, C., Jiang, T., 2017. Impacts of climate change on streamflow in the upper Yangtze River basin. Clim. Chang. 141 (3), 533–546.
Taylor, K.E., Stouffer, R.J., Meehl, G.A., 2012. An overview of CMIP5 and the experiment design. Bull. Am. Meteorol. Soc. 93 (4), 485–498.
Walvoord, M.A., Kurylyk, B.L., 2016. Hydrologic impacts of thawing permafrost—a review. Vadose Zone J. 15 (6).
Wan, Z., 2007. Collection-5 MODIS Land Surface Temperature Products Users' Guide. ICESS, University of California, Santa Barbara.
Wang, T., Wang, N. and Li, S., 2006. Map of the Glaciers, Frozen Ground and Desert in China, 1:4,000,000. Chinese Map Press, Beijing, China.
Wang, T., et al., 2018a. Historical and future changes of frozen ground in the upper Yellow River Basin. Glob. Planet. Chang. 162, 199–211.
Wang, T., Yang, H., Yang, D., Qin, Y., Wang, Y., 2018b. Quantifying the streamflow response to frozen ground degradation in the source region of the Yellow River within the Budyko framework. J. Hydrol. 558, 301–313.
Warszawski, L., et al., 2014. The Inter-Sectoral Impact Model Intercomparison Project (ISI-MIP): project framework. Proc. Natl. Acad. Sci. U. S. A. 111 (9), 3228–3232.
Wu, Q., Hou, Y., Yun, H., Liu, Y., 2015. Changes in active-layer thickness and near-surface permafrost between 2002 and 2012 in alpine ecosystems, Qinghai–Xizang (Tibet) Plateau, China. Glob. Planet. Chang. 124, 149–155.
Wu, X., Nan, Z., Zhao, S., Zhao, L., Cheng, G., 2018. Spatial modeling of permafrost distribution and properties on the Qinghai-Tibet Plateau. Permafr. Periglac. Process. 29 (2), 86–99.
Xu, X., Zhang, Z., Wu, Q., 2016. Simulation of permafrost changes on the Qinghai–Tibet Plateau, China, over the past three decades. Int. J. Digital Earth 1–17.
Yang, M.X., Nelson, F.E., Shiklomanov, N.I., Guo, D.L., Wan, G.N., 2010. Permafrost degradation and its environmental effects on the Tibetan Plateau: a review of recent research. Earth-Sci. Rev. 103 (1–2), 31–44.
Yang, K., et al., 2016. Land surface model calibration through microwave data assimilation for improving soil moisture simulations. J. Hydrol. 533, 266–276.
Zhang, T., et al., 2005. Spatial and temporal variability in active layer thickness over the Russian Arctic drainage basin. J. Geophys. Res. Atmos. 110 (D16).
Zhao, S.P., Nan, Z.T., Huang, Y.B., Zhao, L., 2017. The application and evaluation of simple permafrost distribution models on the Qinghai–Tibet Plateau. Permafr. Periglac. Process. 28 (2), 391–404.
Zhu, Z., et al., 2013. Global data sets of vegetation leaf area index (LAI)3g and fraction of photosynthetically active radiation (FPAR)3g derived from global inventory modeling and mapping studies (GIMMS) normalized difference vegetation index (NDVI3g) for the period 1981 to 2011. Remote Sens. 5 (2), 927–948.
Zou, D., et al., 2017. A new map of permafrost distribution on the Tibetan Plateau. Cryosphere 11 (6), 2527.